

# Chapter 2

## Biological Olfaction Inspired Chemical Sensors

Nan Wang

Olfaction, the sense of smell, is considered to be one of the earliest senses that are highly developed during the course of evolution. This biological system shows astonishing specificity which enables odorant information to be precisely perceived and analyzed by almost all eukaryotes, from invertebrate insects to vertebrate mammals. The internal structure of the olfactory sensing system is arranged in a fascinatingly intricate but intelligent way to ensure both high sensitivity and selectivity towards different chemical molecules. This chapter highlights some artificial sensors and systems that are developed to mimic either the morphological or the functional merits of the olfactory sensing system in terms of optical, gas, and chemical sensing.

### 2.1 Biological Olfactory Sensing System

#### 2.1.1 *Olfactory System of Terrestrial Animals*

Olfactory sensing system, one of the most enigmatic sensing organs, provides fundamental and paramount capability for all eukaryotes to survive in the evolutionary processes. The sense of smell is of particular importance for newborn mammalian cubs to be able to find the teats and obtain their mother's milk to live. As for humankind, odorant sensing is even peculiar as different odors will affect the emotional feelings, with which some distant memories can be evoked. Having the most complex brains in the kingdom of terrestrial animals, the olfactory system of humans is of great interest to scientists and is therefore widely studied [1, 2]. The stunning ability of humans' olfactory system towards odorant detection is attributed to the anatomic structure as well as the nerve network. As shown in Fig. 2.1, the olfactory receptor cells are located in the deep area of the nasal cavity with one end of the neuron dendrites forming columnar micro-sized cilia, protruding out of the

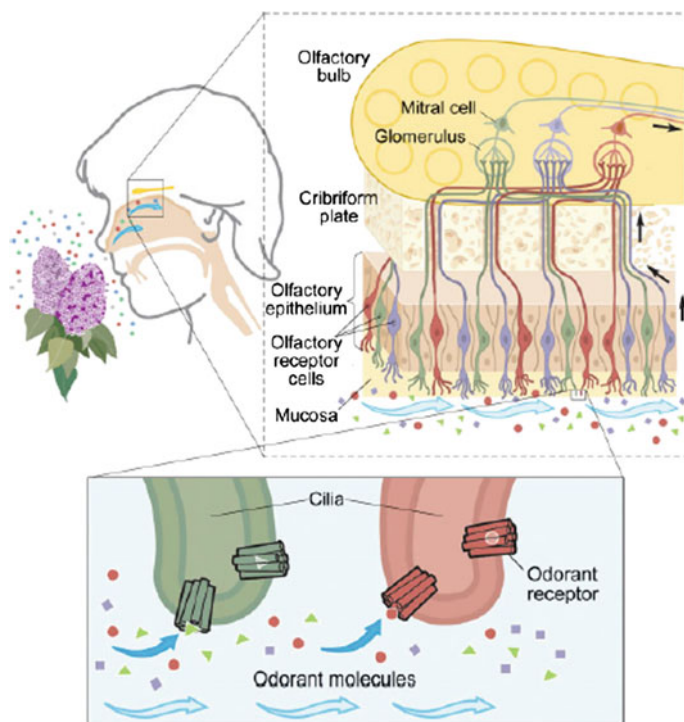


**Fig. 2.1** Schematic representation of human olfactory sensing system, where *black arrows* the processing pathway of the odorant information. Reprinted with permission from Ref. [1]. Copyright: © The Nobel Committee for Physiology or Medicine

surface of the olfactory epithelium. The cilia have tubular structure (odorant receptor) to provide the site for binding of odorant molecules. A mucosa layer is overlying on the epithelium to function as a solvent for the transportation of odorant molecules to the receptors. The other end of the neuron dendrites is projected to the glomeruli, the first ‘information processing unit’ in the olfactory bulb, through the cribriform plate. The information is further converged to the mitral cells, which form synapses with the sensory neurons of glomeruli and also transmit the information to other parts of the olfactory system [1].

The olfactory receptor cells will be activated if a sufficient number of odorant molecules bind to the receptors, the time when electric signals are generated. The signals are firstly processed in the glomeruli, the outer layer of the olfactory bulb, and then nerve endings of the glomeruli will forward the signals to the mitral cells, a region considered to be the inner layer of the olfactory bulb. Finally, the signals with preprocessed odorant information are sent to higher regions of the brain for final processing and storage. Surprisingly, research conducted by Axel and Buck shows that each olfactory receptor cell expresses only one kind of receptor, which can only be triggered by a few types of odorant substances [1]. Besides, olfactory receptor

cells carrying the same kind of receptor transmit the electric signals to the same glomerulus. This fact demonstrates the remarkable specificity developed by the individual olfactory receptor cell can be maintained by the glomeruli and therefore the brain is able to accurately distinguish different odorant signatures even in the situation that certain smell has mixed types of odors. Another interesting point is that one kind of odorant molecule will activate multiple olfactory receptors, indicating the mode that brain encodes odorant information is not in a ‘one by one’ approach but with a combinational pattern. This is the basis for humans’ capability to identify and memorize more than 10,000 odors [1]. Other than incredible specificity, the high sensitivity of olfactory sensing is contributed by the random distribution of a large number of olfactory cilia with different receptors on the surface of the olfactory epithelium as well as the three-dimensional anatomy of olfactory cilia, which significantly increases the surface area that is in contact with inhaled molecules.

The general concept of olfactory transduction mechanism is schematically described in Fig. 2.2, where upon binding to odorant molecules, the olfactory receptor will release the G-protein ( $G_{s(olf)}$ ) inside the cytoplasm. This causes the elevated concentration of cyclic adenosine monophosphate (cAMP) to be synthesized via adenylyl cyclase stimulated by partial structure of the  $G_{s(olf)}$ . The concentration increase further opens the cyclic nucleotide gated channel (CNG channel), generating a high influx of cations (mainly  $Ca^{2+}$ ) to depolarize the cell and then an action potential is produced which will propagate to the olfactory bulb [2]. The amazing part of the olfactory transduction mechanism reveals on the fact that protein chain of the olfactory receptor will undergo a series of transformations to transverse the cell membrane of the cilia several times [1, 2]. The proteins of all odorant receptors share a lot of similar polypeptide chains and have only a small

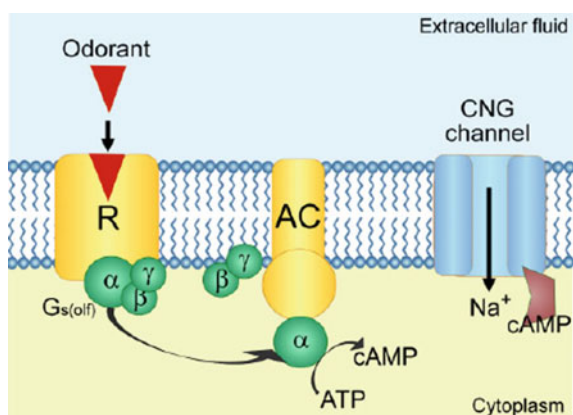


**Fig. 2.2** Schematic representation of the olfactory transduction mechanism upon binding to odorant molecules. Where *R* olfactory receptor, *AC* adenylyl cyclase, *CNG channel*, cyclic nucleotide gated channel, *G<sub>s(olf)</sub>* G-protein, *ATP* adenosine triphosphate, *cAMP* cyclic adenosine monophosphate. Reprinted with permission from Ref. [2]. Copyright (2009) John Wiley and Sons

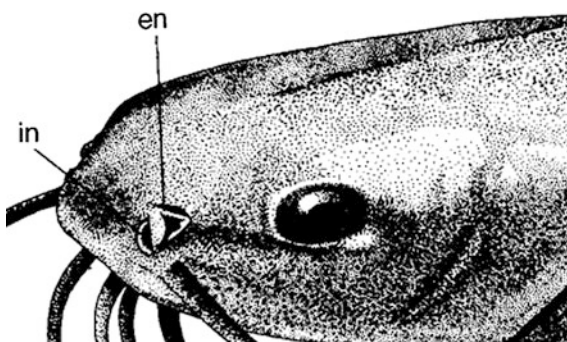
fraction of differences. With such subtle variations, different odorant receptors are still capable of recognizing varieties of odorant molecules [1].

### 2.1.2 Olfactory System of Aquatic Animals

The olfaction system of terrestrial animals is mainly used to detect volatile substances, whereas the olfaction system of aquatic animals, especially fishes, basically serves to perceive fluid-phase substances. For the majority of fishes, the peripheral olfactory system is not easily visible. Typically, it is comprised of a pair of two nasal chambers which are located on the dorsal surface of the head, as shown in Fig. 2.3. When fish moves around in a freshwater or seawater basin, water flowing opposite to their swimming direction will be drawn into the olfactory chamber through the anterior nostril and then will be drained out through the posterior nostril. The interesting point is that most of fish olfactory organs are not connected to their mouth [3], which distinguishes them from air-breathing vertebrates. Generally, large numbers of irregular flexible folds, which are also termed as lamellae, protrude from the floor of the olfactory chamber with sensory epithelium attaching on both sides of each lamella, as shown in Fig. 2.4. The epithelium innervated by olfactory sensory neurons can transmit a signal to the fish brain once enough odorant molecules are captured. The exact number of these lamellae will change with different types of fishes and usually increases to a maximum value as the baby fish grows up gradually [3].

Figure 2.5a shows the schematic nerve layout to illustrate how odorant information is transmitted within the fish olfactory system. At first, odorant molecules will be carried into the olfactory rosette (OR) through forward swimming of fish in water. Then the odorant information is conveyed to the primary sensing area, which is the olfactory bulb (OB) by activating sensory neurons located in the sensory epithelium. Finally, the olfactory tract (OT) will project this information into the higher centre of the brain, i.e. the telencephalon (T), via thousands of axons [4]. Basically, three types of sensory neurons are responsible for detecting odorants,

**Fig. 2.3** Lateral view to show the position of one olfactory organ of sea catfish. Where in, incurrent nostril; en, excurrent nostril. Reprinted with permission from Ref. [3]. Copyright (2010) John Wiley and Sons



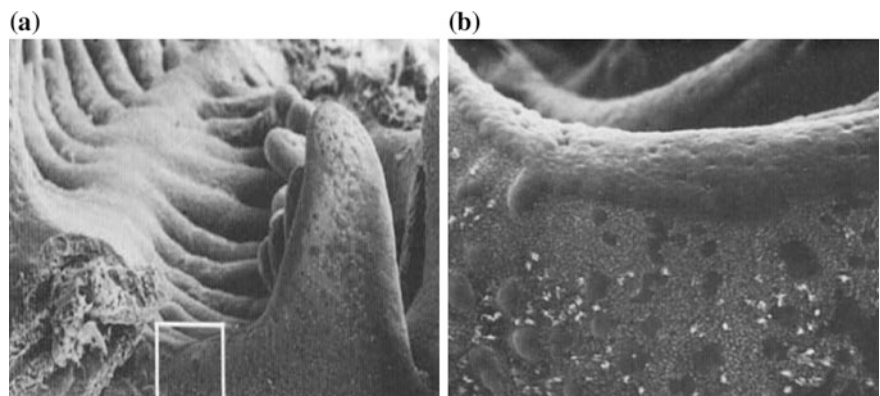
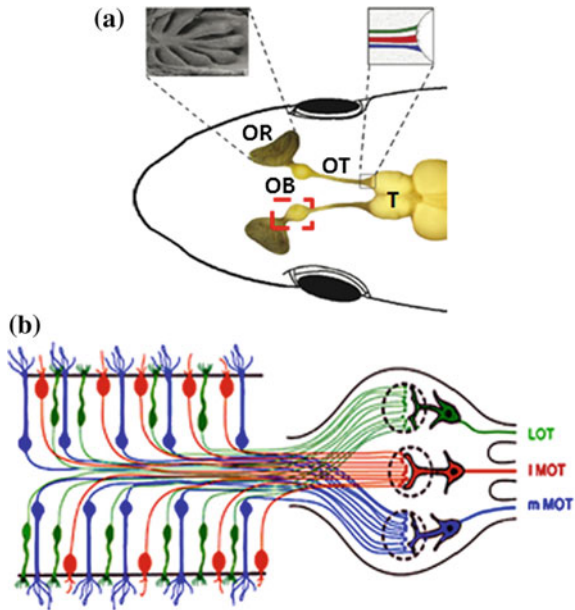


**Fig. 2.4** **a** SEM image of the lamellae within the olfactory chamber of hardhead sea catfish. **b** Enlarged view of the boxed region to show attached sensory epithelium. Reprinted with permission from Ref. [3]. Copyright (2010) John Wiley and Sons

**Fig. 2.5** **a** Schematic diagram of the nerve layout of fish olfactory system. **b** Enlarged drawing of the *red dashed* region to depict three sensing pathways. Where, *OR* olfactory rosette, *OB* olfactory bulb, *OT* olfactory tract, *T* telencephalon, *LOT* lateral olfactory tract, *IMOT* lateral portion of medial olfactory tract, *mLOT* medial portion of medial olfactory tract. Adapted with permission from Ref. [4]. Copyright (2007) Elsevier



which are ciliated sensory cells (shown in blue colour in Fig. 2.5b), microvillous sensory cells (shown in green colour) and crypt cells (shown in red colour). By applying carbocyanine dye to the glomerular region of the olfactory bulb, researchers found that the axons of ciliated sensory neurons, microvillous sensory neurons, and crypt cells terminate at the medial portion of medial olfactory tract (mMOT), lateral olfactory tract (LOT) and the lateral portion of medial olfactory tract (lMOT), respectively [4]. Moreover, electric stimulation of different olfactory tracts will trigger specific reactions for free moving fish. It is confirmed that

irritation of the mMOT, LOT and IMOT separately induce alarm reaction, feeding behaviour and reproductive behaviour [4]. This arrangement exhibits similarities with the olfactory system of air-breathing animals, in which olfactory sensing neurons carrying the same type of odorant information converge to the same olfactory tract. Signals pertaining to different functionalities will be maintained until they reach to the brain in such a way that high specificity towards multiple kinds of odorant molecules can be registered.

Among all classes of the fish group, sharks, a subclass of the *Elasmobranchii*, which is one major category of cartilaginous fish, exhibit extraordinary smelling power in water [5]. They are able to pinpoint one drop of blood in one million drops of water and to identify the location of blood source even from few hundred meters away. Such sensing ability is attributed to the special morphology of the olfactory organ of sharks. In fact, the olfactory organs of sharks demonstrate considerable diversity in position, size and form, which is usually related to their living environment and habitat [5]. Sharks can be categorized into benthic species and pelagic species. Benthic sharks mainly rely on close-range sensing systems like vision as well as electroreception in terms of feeding strategies, since they usually scan the seabed for hidden or slow-moving prey. As a result, they have circular, wider incurrent nostrils, which are located close to the mouth, as shown in Fig. 2.6a, providing broad exposure space to surrounding environment [5]. Conversely, pelagic sharks highly depend on long-range sensing systems, for example acoustic and chemosensory cues, since they often search for food in open and turbid water areas. Consequently, they have longer, oval-shaped incurrent nostrils, which are always far away from the mouth [5], as shown in Fig. 2.6b. Another hypothesis is that as pelagic sharks often swim at much higher speed in comparison with benthic sharks, the impact of water to the sensory organs can be minimized by having such smaller nostril during high speed cruising [5].

Generally, pelagic sharks employ a pitot-like mechanism to direct water into the olfactory rosette as the incurrent nostrils are positioned perpendicular to excurrent

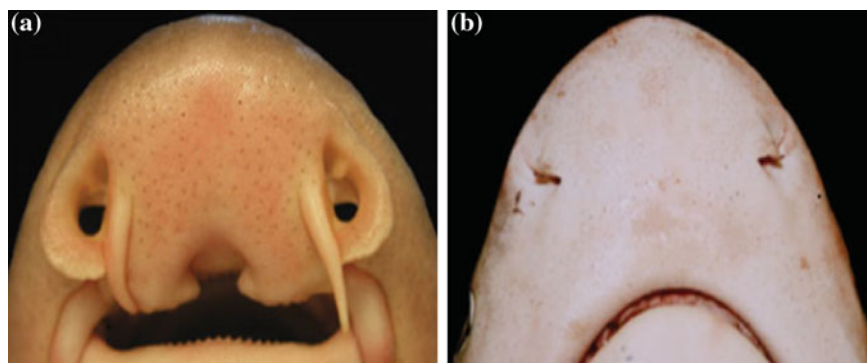


**Fig. 2.6** Ventral view of the olfactory organs of **a** benthic shark—brownbanded bamboo shark and **b** pelagic shark—nervous shark. Reprinted with permission from Ref. [5]. Copyright (2008) John Wiley and Sons



nostrils, resembling a pitot tube. By actively swimming towards upstream current, the pressure difference caused by this pitot arrangement will facilitate water to flow through olfactory cavity [6]. Furthermore, pelagic sharks own streamlined head shape with nostrils situating at the tip of the rostrum, leading to thinner boundary layer generated at the interface between moving fluid and the olfactory organ, which could remarkably reinforce the transport of odorant molecules to sensing regions [6]. However, the olfactory organization of benthic sharks operates similarly to a pump in that it is connected to the respiratory system. By aid of the respiration activity, water is pulled into the olfactory cavity for ventilation, which has much less efficiency in terms of the collection of odorant molecules [6]. Besides, pelagic sharks have a heavier olfactory rosette and larger surface area of the olfactory epithelium, compared to benthic sharks, demonstrating that the morphological shape of the olfactory system is predominantly oriented by the pressure coming from preferred habitat in the course of evolution [5]. On the whole, pelagic sharks develop more advanced and acute chemoreception capability than benthic sharks [5, 6].

Figure 2.7a depicts the internal anatomy of the olfactory rosette of the lemon shark (one representative kind of pelagic sharks) [7]. Olfactory rosette is the place where odorant information is initially generated through intimate contact between odorant molecules and the olfactory sensing neurons. It can be observed that two rows of olfactory lamellae (ol), starting from a central raphe (r) to the dorsal cavity wall (cw), resemble a leaf-like olfactory rosette. As for each olfactory lamella, its outer margin sticks with the interior surface of the olfactory cavity, whereas inner lamellar margin (im) has free circular edge, constituting an inlet chamber (ic) by parallel arrangement, as shown in Fig. 2.7b. Close to the middle part of the olfactory rosette, secondary folds (sf) are often visible with which the total surface area of lamellae can be greatly increased. A curved peripheral canal (pc) exists between the outer margin of lamellae and the inner wall of the cavity [7]. When sharks move forward in the sea, a pressure difference is created between the incurrent nostril and the excurrent nostril. Under the action of this differential pressure, water will be guided to the inlet chamber through the entrance of the incurrent nostril, after which the water begins to automatically spread into the gap system constructed by facing lamellae. Subsequently, water will be drained to the outlet chamber via the peripheral canal and be discharged by the opening of the excurrent nostril. An odorant signal is produced at the time when water goes into the gap system and touches with every lamella [7].

The side wall of each lamella is covered by large numbers of bundles of sensory epithelium and non-sensory epithelium, as shown in Fig. 2.7c. These epithelia possess laminated columnar standing configuration with higher density, smaller diameter and shorter height of the non-sensory epithelium compared to the sensory epithelium [7]. However, the sensory epithelium covers more surface area than the non-sensory one. According to the histological study of the olfactory lamella, abundant microvillous sensory cells which are corresponding to odorant sensing, situate among the sensory epithelium [7]. Interestingly, in complete contrast to fishes, researchers report that almost all shark species have no ciliated sensory cells [5, 7], which are linked to the alarm reaction. Such findings may be interpreted by the fact that the

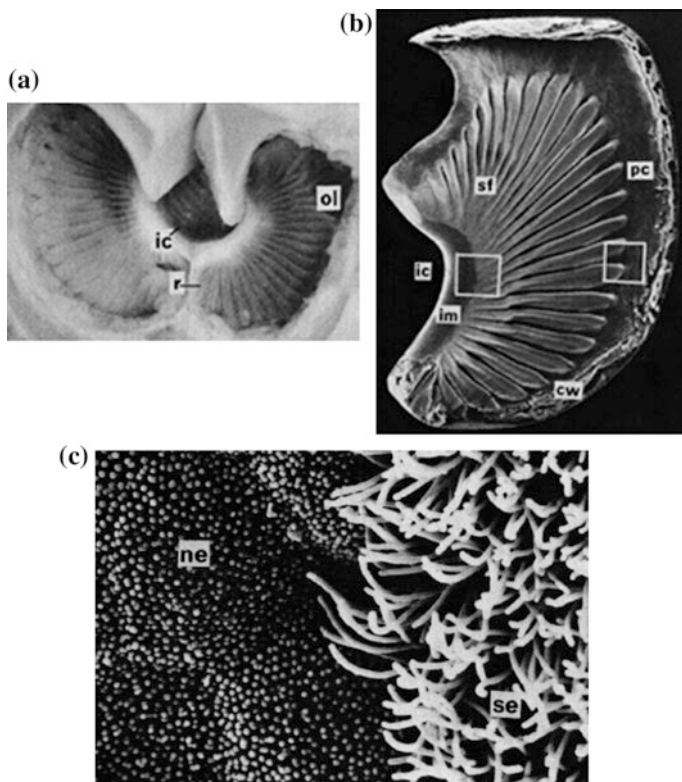


**Fig. 2.7** **a** Cross-sectional SEM image of the olfactory rosette of the lemon shark. **b** Enlarged SEM image to show detailed anatomical structure of the olfactory rosette. **c** SEM image with high magnification to show the sensory epithelium (se) and the nonsensory epithelium (ne). Where, *ic* inlet chamber, *r* raphe, *ol* olfactory lamella, *sf* secondary fold, *pc* peripheral canal, *im* inner lamellar margin, *cw* cavity wall. Reprinted with permission from Ref. [7]. Copyright (1987) NRC Research Press

majority of sharks are predators rather than prey owing to their giant body size. The stratified distribution of sensory epithelium on the side wall of the olfactory lamellae tremendously augments contact probabilities between the odorant molecules and the olfactory receptors. Such a unique feature of the olfactory system significantly boosts the sensing capability of pelagic sharks to odorant message [5, 7].

## 2.2 Artificial Sensors Inspired by the Olfactory System of Terrestrial Animals

Nature can serve as a source of inspiration for human beings to design novel devices emulating the function of animals, while at the same time exploring its beauty and mystery. The survival instinct combined with the evolutionary processes



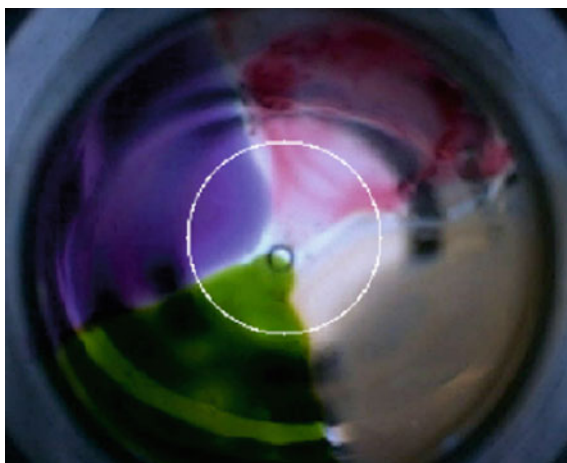
impels different creatures to develop ultrasensitive sensors. It is of great interest to develop artificial counterparts to mimic these high-performance biological sensors [8–12]. Research touching on this exhilarating topic has just begun and tremendous detailed information is still scarce.

### 2.2.1 Olfactory Glomeruli Inspired Optical System

In the biological olfactory sensing system, odorant information collected by olfactory receptor neurons is initially converged into the glomerular regions. It is surprising that the number of glomeruli (about 6 million for humans) is a few thousand times less than the number of olfactory receptor neurons (about 2 thousand times for humans), suggesting that biological olfactory system has a highly smart and strategic organization of the nerve wiring network [1]. Inspired by this captivating arrangement, an artificial olfactory system based on optical imaging was proposed by Natale et al. [13] to mimic the convergence properties of the olfactory receptor neurons. The system was built by sandwiching a polyvinyl chloride (PVC) film, which contains four color indicators as sensing molecules [i.e. 5,10,15,20-tetraphenylporphyrin zinc (ZnTPP), 5,10,15,20-tetraphenylporphyrin manganese chloride (MnTPP), 5,10,15,20-tetraphenylporphyrin cobalt (CoTPP), and 5,10,15,20-tetraphenylporphyrin platinum (PtTPP)], with two plastic coverslips, as shown in Fig. 2.8. The upper coverslip has a hole to allow odorant molecules to diffuse into the film and interact with different porphyrinoid indicators.

Upon exposing vapors of different chemicals to the sensing film, an image (7845 pixels in total) with an arbitrary shape of color indicators was created by illuminating a controlled light source. The optical characteristics of each pixel in the image were recorded by a standard digital camera and treated as the optical

**Fig. 2.8** Photograph of an artificial olfactory system based on optical imaging, which is made of a PVC sensing film with four color indicators. The white circle shows the region of the image with 7845 pixels captured by a standard digital camera. Reprinted with permission from Ref. [13]. Copyright (2009) Elsevier



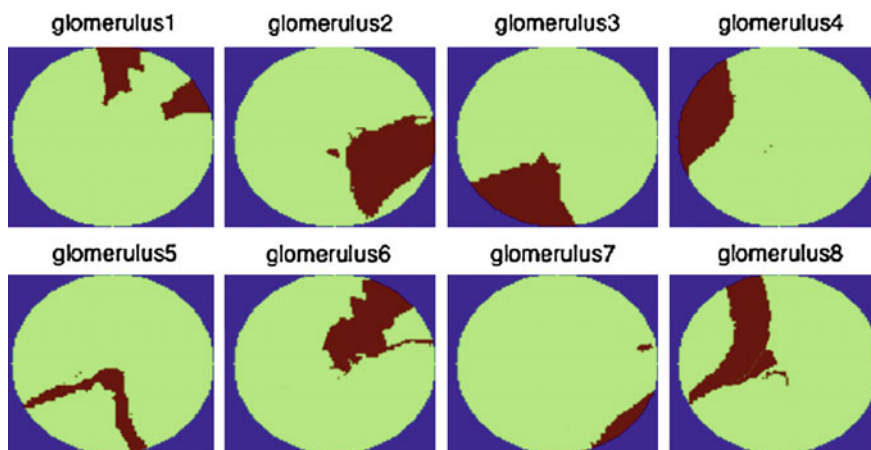


**Fig. 2.9** Captured images to show the convergence of different porphyrinoid indicators into eight artificial glomeruli. Where, glomeruli 1 and 6 correspond to ZnTPP; glomeruli 2 and 7 correspond to PtTPP; glomeruli 3 and 5 correspond to MnTPP; glomeruli 4 and 8 correspond to CoTPP. Reprinted with permission from Ref. [13]. Copyright (2009) Elsevier

fingerprint of the pixel which reflects both the nature of the porphyrinoid indicators and its quantity dispersed into the sensing film. In the beginning, the sensing film was shined by a color sequence of pure red, pure green and pure blue to define the optical fingerprint of each pixel. Then fingerprints having the same type of optical information were grouped into eight artificial glomeruli by using an unsupervised k-means classifier [13], as shown in Fig. 2.9. In this work, each pixel of the captured image can be considered as an artificial olfactory receptor neuron. The optical fingerprints of different pixels can be described as abstract representations of different olfactory receptors. With the aid of eight artificial glomeruli, optical information of 7845 pixels was expressed in an analogical way that millions of biological olfactory neurons convey the information to few hundreds of glomeruli. Having this artificial olfactory system, the authors demonstrated its capability to distinctly detect four kinds of gaseous chemicals (ethanol, triethylamine, toluene, and butylamine) by analyzing the glomerular signals with the lateral inhibition algorithm [13].

### 2.2.2 Olfactory Mucosa Inspired Gas Sensor Array

As previously mentioned, the olfactory sensory epithelium is covered by a layer of fluidic mucosa with cilia of olfactory receptor cells extending into the layer. The function of the mucosa is to provide a liquid environment for odorant molecules to dissolve and subsequently to be captured by olfactory receptors. In addition, the mucosa also plays the role of filtering large particles and adventurous impurities that could possibly damage the olfactory cilia [1]. Inspired by this biological

arrangement, a gas sensor array was proposed by Wang et al. [14], in which a layer of multiple-walled carbon nanotube (MWNT) was deposited as the electrode layer on the silicon substrate and a layer of polymer film was formed onto the MWNT layer, establishing a bilayer structure similar to the olfactory mucosa. The authors selected eight kinds of polymers, i.e. styrene/allyl alcohol copolymer (SAA), polyvinylpyrrolidone (PVP), poly(vinylidene chloride-co-acrylonitrile) (P(VDC-AN)), poly(methyl vinyl ether-alt-maleic acid) (PMVEMA), poly(alpha-methylstyrene) (PMS), hydroxypropyl methyl cellulose (HPMC), poly(ethylene adipate) (PEA), and poly(vinyl benzyl chloride) (PVBC), based on the linear solvation energy relationship theory as well as the physical absorption bonding to enhance the response of the sensor array towards different odors. A bio-inspired fast-adaptive readout circuit was also incorporated into the system which has two operating modes (calibration and sensing) with different time constants. The circuit is able to quickly perform the calibration with a small time constant and then switch to the sensing mode with a large time constant, which duplicates the feature of biological olfactory sensing system in the way that upon being contact with an unknown odor stimulus, it will give a quick response in the initial stage and later on adapt to the odor [14].

The artificial mucosa bilayer sensing film showed much better performance in terms of higher sensitivity, faster recovery time and more repeatable response compared with the single-layer sensing film, which was fabricated by drop casting the mixture of MWNTs and polymers dissolved in the methyl ethyl ketone solution [14]. Improvements of detection capabilities revealed by bilayer film are attributed to the surface topography, where only polymer is present at the top surface of the bilayer sensing membrane. In contrast, the superficial structure of single-layer film has a lot of MWNTs exposed to disrupt the membrane, resulting in a partial blocking of the polymer pores. Therefore, the polymer-only film has higher sensitivity due to more surface area provided to facilitate the absorption together with desorption process of the target gas. Moreover, the diffusion length of the absorbed gas into the sensing polymer is also shortened to speed up the recovery time as the gas can be in direct contact with the sensing membrane [14]. Figure 2.10 demonstrates the fantastic ability of the mucosa-inspired sensor array to distinguish three different odors of alcohols, i.e. sake, sorghum liquor and whisky, which have comparable chemical compositions [14].

### 2.2.3 *Olfactory Receptor Protein Inspired Gas Nanosensor*

As reported [15], there are approximately 1000 different genes, which accounts for nearly 3 % of the total number of humans' genes, associated with odor discrimination in mammals. Upon binding to olfactory receptor proteins, the molecular feature of the odor is analyzed by different olfactory receptors expressing unique genes. High-specific odor recognition is achieved by using a combinatorial manner [15], as shown in Fig. 2.11, in which different odorant molecules are captured by

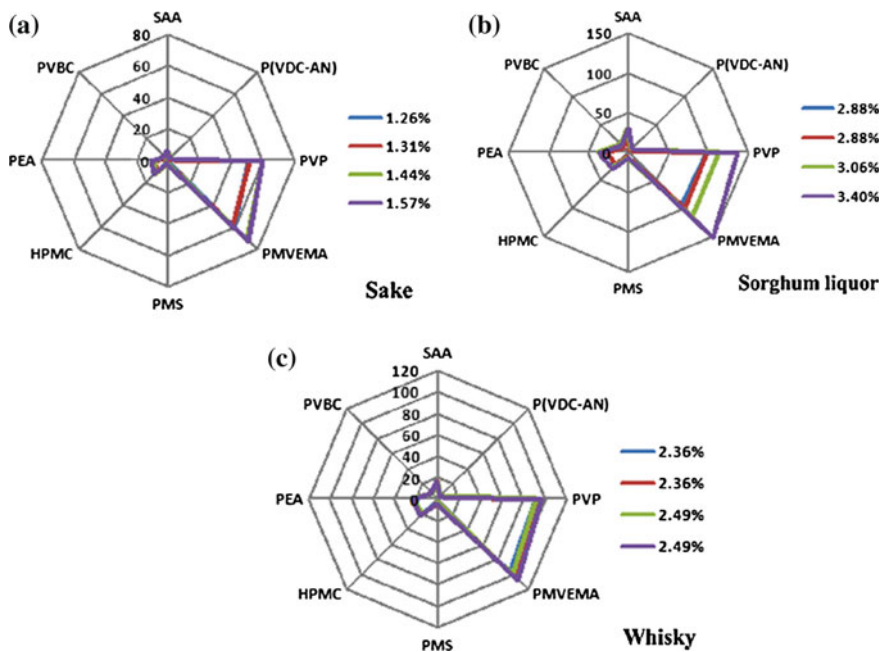


**Fig. 2.10** Radar plots to show the detection of **a** sake, **b** sorghum liquor and **c** whisky under different concentrations by using mucosa-inspired gas sensor array. Reprinted with permission from Ref. [14]. Copyright (2011) Elsevier

Odorant receptors	1	2	3	4	5	6	7	8	9	10	11	12	13	14	Description
<b>Odorants</b>															
<b>A</b> 															rancid, sour, goat-like
<b>B</b> 															sweet, herbal, woody
<b>C</b> 															rancid, sour, sweaty
<b>D</b> 															violet, sweet, woody
<b>E</b> 															rancid, sour, repulsive
<b>F</b> 															sweet, orange, rose
<b>G</b> 															waxy, cheese, nut-like
<b>H</b> 															fresh, rose, oily floral

**Fig. 2.11** The combinatorial manner of forming olfactory perceptions through different combinations of the olfactory receptors when subjecting to different odorant molecules. Reprinted with permission from Ref. [15]. Copyright: © The Nobel Committee for Physiology or Medicine

different combinations of the olfactory receptors, thereby generating different codes. These codes, in the form of neurological signals, are subsequently interpreted by the brain to form odorant perceptions as well as to recall related memories. With such complex and hierarchical sensing configuration, most mammals are capable of distinguishing more than 10,000 odors even at very low levels of a few parts-per-billion [15].

Attracted by such captivating binding specificity of the olfactory receptor proteins, over the past, attempts have been made to develop gas sensors integrated with biomolecules to garner binding capability similar to the olfactory sensing system, among which peptides are of particular interest due to their chemical properties and robustness in extreme conditions. Cui et al. [16] reported the development of gas nanosensors by coupling peptides to nanomaterial surfaces (Fig. 2.12a) to achieve sensitive and selective detection of biochemical molecules in the mixtures of vapors. They selected antennal-specific protein-1 (ASP1), one kind of odorant binding proteins of the honeybee (*Apis mellifera*), as the recognition element. The ASP1 has four amino acid residues that show strong binding affinity to trinitrotoluene (TNT). The authors examined the immobilization of two peptides, namely graphene binding peptide (GBP: amino acid sequence EPLQLKM) and carbon nanotube binding peptide (CBP: amino acid sequence HSSYWYAFNNKT) on the nanomaterial substrate. Besides, the authors also predicted the structure of the peptide using the molecular dynamics simulations, as shown in Fig. 2.12b, after interaction between the bifunctional peptide (consists of a single-walled carbon nanotube binder and an ASP1C TNT binder) and the carbon nanotube [16]. They estimated the interaction energy to be about 9 kcal/mol, which suggests a significant enhancement of the binding capability towards TNT molecules [16]. As shown in Fig. 2.12c, upon exposing to 12 ppb TNT, the nanosensor after functionalizing of the peptide (ASPC1) onto the graphene exhibits a much stronger decrease in drain-source current compared to the sensor with bare graphene and the one with GBP. An experiment performed by sequentially flowing acetic acid (AcOH) and ammonia (NH<sub>3</sub>) gases under a background of 6 % CO<sub>2</sub> with two nanosensors modified by AcOH and NH<sub>3</sub> peptide sequences, as shown in 2.12d, demonstrates high sensitivity and selectivity of the biomimetic functionalized nanosensors for odorant detection [16].

### 2.2.4 Olfactory Sensilla Inspired Nanopores

The olfactory organs of most insects are located in the third segment of the antenna as well as the section of the maxillary palp [17], as shown in Fig. 2.13a. These chemosensory organs are protected by the sensory sensilla which have different morphologies, e.g. basiconic, coeloconic and trichoid shapes [17]. The olfactory receptor cells of insects share a similar structure with vertebrate ones with the apical end of the neuron protruding into the lymph of the individual sensillum to form olfactory dendrites and the other end of the neuron forming basal axon to transmit

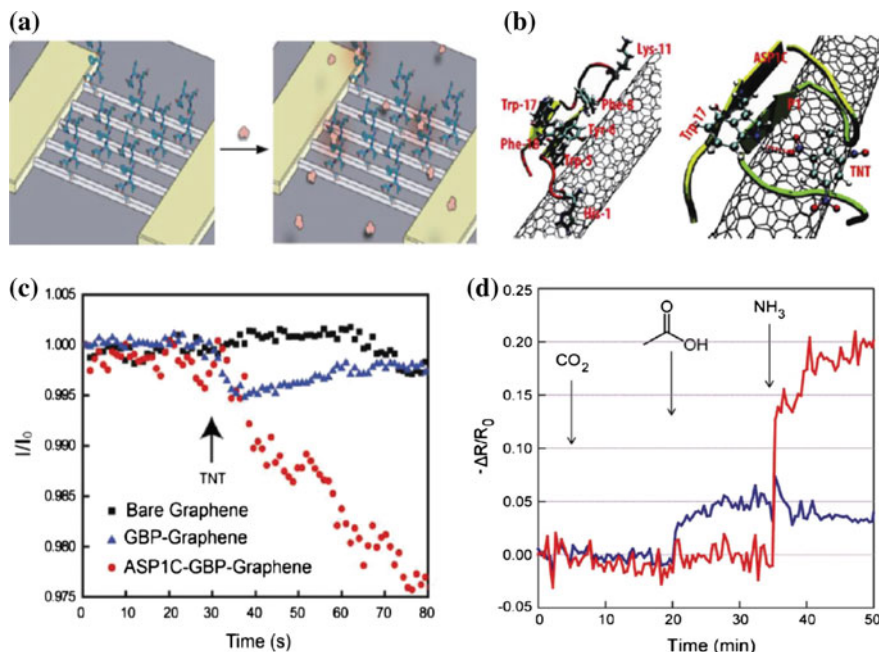


**Fig. 2.12** **a** Schematic drawing to show the detection of target molecules by peptide sequences immobilized on the nanosensor. **b** Prediction of the peptide structure after interaction between the bifunctional peptide and the carbon nanotube. **c** Response of different nanosensors after exposing to 12 ppb TNT. **d** Response of the peptide sequences modified nanosensors to the flow of AcOH and  $\text{NH}_3$  gases under  $\text{CO}_2$  background. Reprinted with permission from Ref. [16]. Copyright (2012) American Chemical Society

olfactory signal to the glomerulus located in the antennal lobe, as shown in Fig. 2.13b. The olfactory signal is generated through binding of airborne volatile molecules/pheromones to different olfactory receptors. The pheromones are believed initially to be captured by the lipid-coated nanopores that are scattered on the surface of the sensilla. This lipid layer also significantly contributes the concentration and translocation of odorant molecules to the dendrites of the olfactory receptors [17].

Inspired by the alluring multi-functionality of lipid-coated nanopores, Yusko et al. [18] reported the design of synthetic nanopores coated with fluid lipid bilayers for molecular analysis of single proteins, as shown in Fig. 2.14a. Experiments with nanopores are able to provide detailed information about the size, composition, and activity of small/single molecules. The fluid bilayer on the nanopore's sidewalls was created by exposing the nanopore fabricated on a silicon substrate to unilamellar liposomes and the properties of the coating layer were finely adjusted in terms of thickness and surface chemistry. The diameter of the nanopores was dynamically varied ( $1.4 \pm 0.1$  nm [18]) by using thermal phase transition of the selected lipids, which could enable the nanopore-based experiments to have higher sensitivity, thus revealing more important information about the tested molecule.



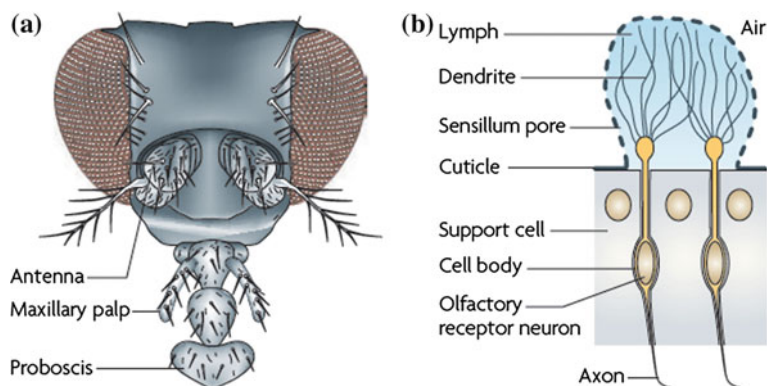


**Fig. 2.13** **a** Schematic drawing of the head of insects to show the location of the antenna and the maxillary palp. **b** Schematic drawing of the anatomical structure of one sensillum. Reprinted with permission from Ref. [17]. Copyright (2010) Nature Publishing Group

Such mechanism of tuning nanopore's diameter mimics the capability of insects to control the water absorption and evaporative desorption. The authors also modified the bilayer with functionalized ligands, as shown in Fig. 2.14b, to enhance the accumulation of dilute analytes and to discriminate different analytes by recording the frequency of the translocation events [18]. The fluidic nature of the bilayer reduces the non-specific capture of other kinds of molecules, with which the relationship between the translocation times and the charge of the molecules can be quantitatively derived. In addition, high viscosity of the coated bilayer further slows down the translocation events of the target molecules, making it possible to

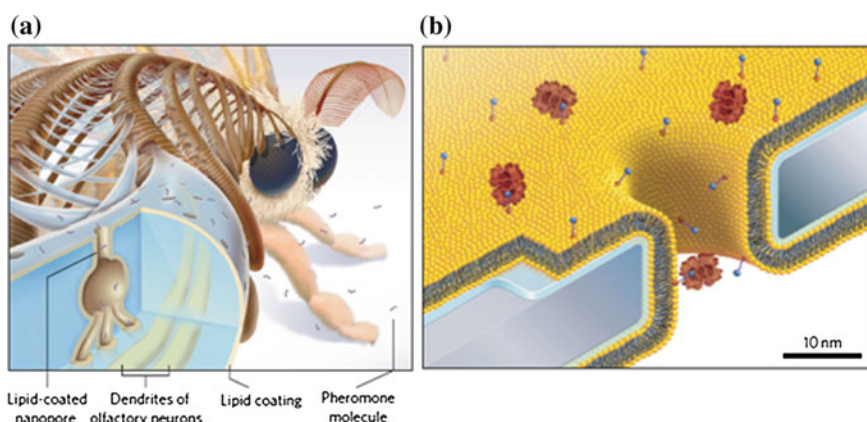


**Fig. 2.14** **a** Schematic drawing of the lipid-coated nanopore present on the sensillum of silk moth's antenna. **b** Schematic drawing of the fluid lipid bilayer coated nanopore modified with the functionalized ligands. Reprinted with permission from Ref. [18]. Copyright (2011) Nature Publishing Group

determine the time-resolved translocation time and the amplitude of the resistive pulses. With the proposed fluid lipid bilayer coated nanopore, the molecular volume and the shape of the target proteins can be quantitatively analyzed. The authors successfully validated their hypotheses by experimentally estimating the molecular volume of three different proteins, i.e. streptavidin ( $94 \pm 18 \text{ nm}^3$ ), polyclonal Fab fragments ( $172 \pm 31 \text{ nm}^3$ ) and monoclonal antibodies (between  $308$  and  $696 \text{ nm}^3$ ) and the net charge of two different proteins, i.e. polyclonal Fab fragments (between  $-2.9$  and  $-5.3$ ) and monoclonal antibodies ( $-4.2 \pm 0.5$ ) [18].

## 2.3 Artificial Sensors Inspired by the Olfactory System of Aquatic Animals

### 2.3.1 Bio-inspired Sensor Design

Although progress has been made in the detection of air-borne odorant molecules using sensors inspired by the terrestrial animals' olfactory system, in terms of sensitivity and selectivity, relatively little research is done pertaining to the development of artificial sensors to mimic the olfactory system of aquatic animals. Wang et al. [19] proposed a MEMS chemical sensor to biologically imitate the morphological and functional merits of the olfactory sensing system of pelagic sharks for the sake of on-site and/or in situ monitoring of heavy metal contamination. The sensor consists of two parts as shown in Fig. 2.15a, where the top part is a microfluidic channel serving as a holder for water sample as well as a chamber for electrochemical reaction. While the bottom part is a sensor base to place three types of miniaturized electrodes (i.e. working, reference and counter electrodes) along with contact pads for applying potential input via reference and working electrodes and collecting current output through working and counter electrodes. Fabrication of the sensor started from depositing of silicon dioxide ( $1 \text{ }\mu\text{m}$ ) on the silicon substrate (about  $500 \text{ }\mu\text{m}$ ) by using plasma-enhanced chemical vapor deposition to provide insulation for the electrodes. A layer of chromium ( $50 \text{ nm}$ ) was sputtered by using magnetron sputtering system to promote the adhesion between silicon dioxide layer and the upper electrode layer. A layer of gold ( $300 \text{ nm}$ ) was subsequently attached to form the bottom electrode layer and a layer of silver together with silver chloride ( $500 \text{ nm}$ ) was evaporated on the inner semicircle of the gold layer to function as a reference electrode. Thereafter, a layer of SU-8 ( $120 \text{ }\mu\text{m}$ ) was patterned on the middle semicircle of the bottom electrode layer, constituting rigid cores for the micropillar electrode array. A thin film layer of gold ( $200 \text{ nm}$ ) was then coated on the top and side surfaces of all the micropillars to function as working electrode array. The outer semicircle of the bottom gold layer was used as a counter electrode. Finally, the microfluidic channel molded by pouring polydimethylsiloxane (PDMS) onto the SU-8 based structure was bonded on the sensor base. Figure 2.15b depicts the bio-inspired MEMS chemical sensor

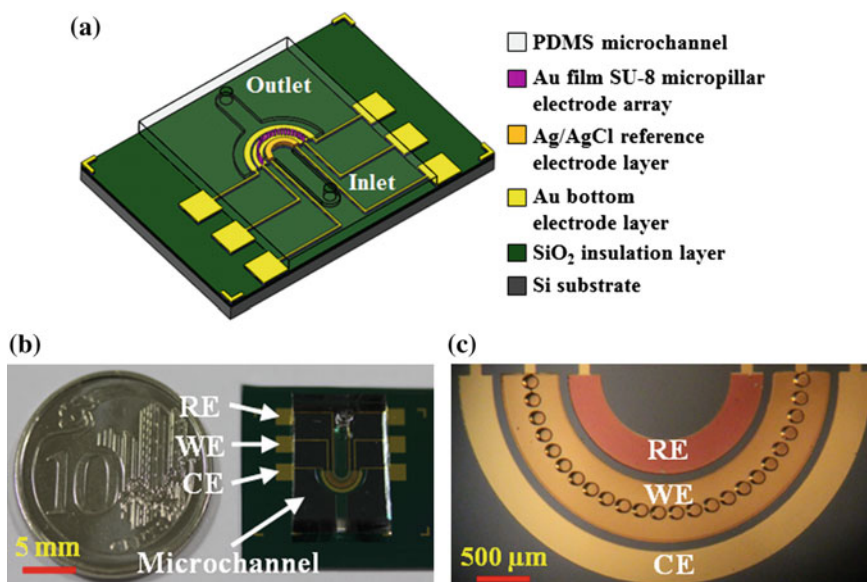


**Fig. 2.15** **a** Schematic drawing of the proposed shark-inspired MEMS chemical sensor to show multiple structural layers [19]. **b** Photograph of the shark-inspired MEMS chemical sensor after fabrication [20]. **c** A close-up of the micropillar working electrode array under an optical microscope [20]. Where, *RE* reference electrode, *WE* working electrode, *CE* counter electrode. Reprinted with permission from Ref. [19]. Copyright (2015) IEEE

after fabrication, where an optical image of the three-dimensional micropillar working electrode array is shown in Fig. 2.15c.

The working procedure of the MEMS chemical sensor can be described as follows. In the first place, a sample solution containing varieties of heavy metal ions is pumped into the reaction chamber through the inlet of the microfluidic channel. Then specific metal ions will electroplate on the working electrode during a deposition step which is controlled by the applied potential and the deposition time. At this point, the inlet of the channel is constrained so that new sample of solution cannot flow into the chamber. The purpose of performing such practice is not only to minimize the volume of required sample, but to provide sufficient time for the heavy metal ions to be absorbed onto the surface of the working electrode. After that, oxidation of target metal ions is triggered by applying potential of opposite polarity with respect to the deposition potential. Within this stripping step, a peak in the current output signal at certain potential in which the species begin to be oxidized will be registered. Finally, this signal is converted to the value of the concentration of the concerned heavy metal ions.

As shown in Fig. 2.16a, the working electrode of the chemical sensor is purposely designed to have numbers of standing micropillars with top and side surfaced being coated by sensing material. Such idea of developing miniaturized micropillar working electrode array is intended to mimic the morphology of

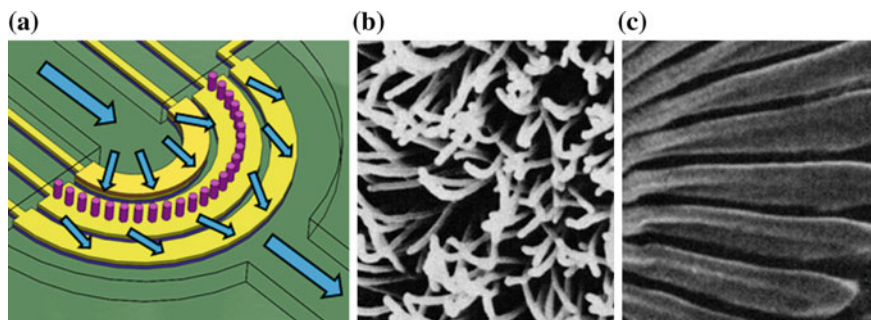


**Fig. 2.16** **a** Schematic drawing to show the solution pathway in the reaction chamber of the shark-inspired MEMS chemical sensor. **b** SEM image to show the olfactory sensory epithelium of the lemon shark [7]. **c** SEM image to show the gap system in the olfactory rosette of the lemon shark [7]. Reprinted with permission from Ref. [7]. Copyright (1987) NRC Research Press

the olfactory sensory epithelium of the lemon shark, as shown in Fig. 2.16b. By incorporating this high-density standing structure into the chemical sensor, effective sensing area that is in contact with the testing solution will be enormously increased, thereby enhancing the sensitivity of the MEMS chemical sensor. Design of the microfluidic channel is aimed at biologically mimicking the arrangement of the gap system constructed by facing lamellae in the olfactory rosette, as shown in Fig. 2.16c. For the lemon shark, when water is sucked into the olfactory rosette under the effect of pressure difference, it will immediately spread along the inter-space of two neighboring lamellae [7]. One outstanding hydrodynamic advantage of such structure is that more lamellae will contribute to the detection of odorant information since sensory epithelia that are attached on the side wall of each lamella can give full play to their competence, maximizing the olfactory sensing efficiency. In a similar manner, when the sample solution is pumped into the inlet passage of the microfluidic channel, it will be directed to those subchannels formed by adjacent micropillars, as depicted in Fig. 2.16a with blue arrows, so that all micropillar working electrodes are able to participate in the process of metal-ion collection. Such biomimetic approach will maximize the sensing capability of the MEMS chemical sensor in terms of ion-capture efficiency as well as ion-detection sensitivity.

### 2.3.2 CFD Simulation with the Sensor

In order to preliminarily confirm our hypotheses, simulation with the proposed shark-inspired MEMS chemical sensor was firstly performed by using the Computational Fluid Dynamics (CFD) ANSYS Fluent software package. The sensor's structure was built in the SolidWorks 2014 as shown in Fig. 2.17, where the microfluidic channel consists of inlet (in blue), outlet (in green), top wall

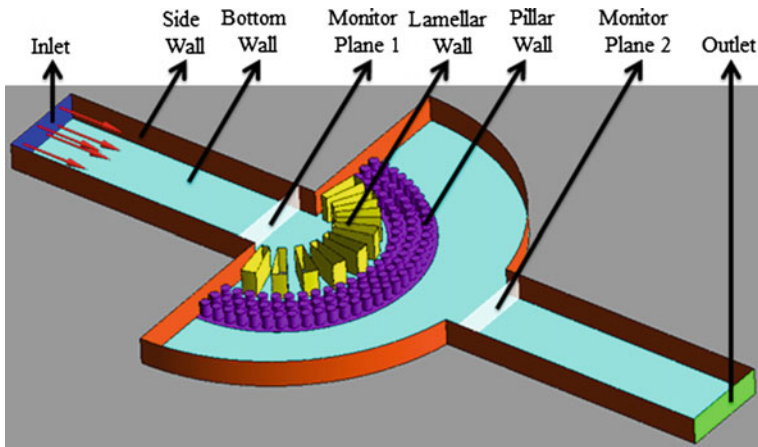


**Fig. 2.17** The geometry of the proposed shark-inspired MEMS chemical sensor built for CFD simulation, where top wall of the microfluidic channel is removed to show internal configuration

(removed to display internal configuration), bottom wall (in azure), side wall (in orange), and lamellar wall (in yellow). The pillar wall (in purple) represents the micropillar working electrode array to function as absorptive sites for heavy metal ions dissolved in the water solution. Monitor plane 1 along with monitor plane 2 (in white) is used to monitor species flux that is penetrating across these two sections for the calculation of the total amount of ion species captured by the working electrode.

Hereafter, the geometry was imported to ANSYS Workbench to mesh for the finite element calculation. The sensor's geometry was primarily meshed with tetrahedron elements under patch conforming algorithm, as shown in Fig. 2.18a, b. Global element size was defined as 0.05 mm which is roughly equal to one sixth of the channel height. Moreover, five layers of inflation with 1.2 growth rate under smooth transition option were applied to the top wall, bottom wall as well as side wall. Lamellar wall and pillar wall were also included since they are all solid immovable objects. By doing so, boundary layer effect produced between the side wall of each micropillar and the flowing solution can be taken into account. Considering the point that flow pattern will be affected by the presence of the micropillar working electrode array, the region which contains the pillar wall was further refined by reducing localized meshing size to 0.02 mm as shown in Fig. 2.18c in view of increasing computational accuracy. Before conducting fluid dynamic simulation, the overall meshing quality of the sensor's structure was carefully checked with some critical criteria such as element quality, aspect ratio, warping factor and skewness to ensure the calculation error induced by poor and inadequate meshing would be minimized.

Fluent simulation of the proposed sensor was performed with pressure-based steady-time solver by activating laminar flow together with the species transport



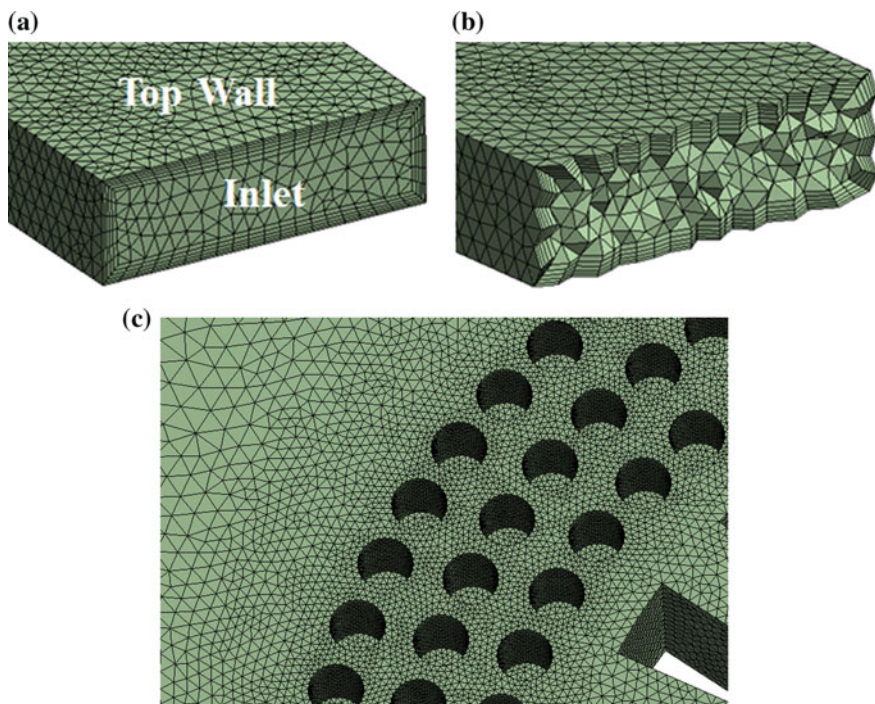


**Fig. 2.18** **a** Meshing of the sensor's geometry and **b** cross-sectional view to show the tetrahedron element and the inflation layer. **c** Meshing refinement of the region which contains the pillar wall

mathematical model. Under this condition, mass conservation equations and momentum conservation equations will serve as the governing equations for the computation of the laminar flow, whereas a three dimensional convection-diffusion equation was employed to predict the mass transport of the chemical species. The fluid injected into the microfluidic channel was a liquid mixture of water and lead nitrate ( $\text{Pb}(\text{NO}_3)_2$ ). Material properties such as specific heat, thermal conductivity and dynamic viscosity of the mixture were specified by using standard values of the water since simulation was targeting on minute concentration range (mainly at ppb level), which means only a tiny amount of lead nitrate is existing in the mixture solution. Density of the mixed fluid was approximated by the volume-weighted-mixing law where water was assigned as the bulk species. Boundary conditions of the simulation were specified as following, where top wall, bottom wall, side wall, lamellar wall and pillar wall are all stationary with no-slip shear condition and zero diffusive flux except for pillar wall which has zero species mass fraction. The inlet and outlet of the microfluidic channel were defined by velocity magnitude with  $1 \mu\text{g/L}$  lead nitrate concentration and gauge pressure with  $0 \mu\text{g/L}$  lead nitrate concentration, respectively. CFD simulation was started by computing fluidic parameters from the inlet initial values.



The first simulation was to investigate the effect of the micropillar working electrode array on species capture efficiency in the microfluidic channel. Figure 2.19a and 2.19b show the schematic drawings, in which Design A1 has a piece of flat working electrode embedded at the bottom wall of the microfluidic channel. Design B1, on the other hand, consists of micropillar working electrode array placed on top of the flat electrode. Height of the microfluidic channel was kept as 0.1 mm for both cases. Simulation results with three inlet velocities (1, 10 and 20 cm/s) are illustrated in Fig. 2.19c. It is indisputable that species capture efficiency is significantly enhanced by 3.56, 4.11 and 4.23 times comparing the sensor with and without micropillar working electrode array, when the inlet velocity is fixed as 1, 10 and 20 cm/s, respectively. Another pronounced phenomenon can be observed from the simulation is that species capture efficiency of the sensor without micropillar electrode array is decreased by 4.5 times when the inlet velocity rises from 1 to 10 cm/s. However, for the sensor with micropillar electrode array, species capture efficiency is only dropped by 3.9 times. The difference of efficiency

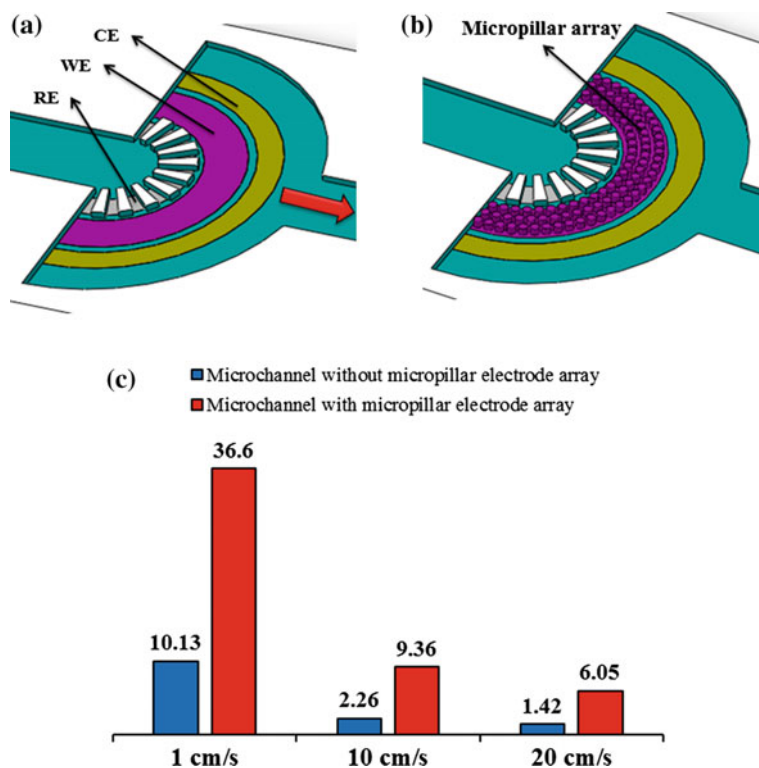


**Fig. 2.19** Schematic drawings of the first simulation using **a** Design A1 and **b** Design B1, where *CE* counter electrode, *WE* working electrode, *RE* reference electrode. **c** Comparisons of species capture efficiency in terms of percentage (%) for the simulations under different inlet velocities

descending becomes even larger, i.e. 7.18 and 6.05 times for the sensor without and with micropillar electrode array upon the inlet velocity reaches to 20 cm/s.

The second simulation was to study the relationship between the height of the micropillar working electrode array and the species capture efficiency in the microfluidic channel. As shown in Fig. 2.20a, microfluidic channels of 0.1, 0.2 and 0.3 mm height were designated to Design A1 and B1, Design A2 and B2, and Design A3 and B3, respectively. For Design B1, B2 and B3, the height of the micropillar working electrode array is identical with the height of the microfluidic channel. Figure 2.20b shows the simulation results, in which species capture efficiency is prominently amplified for the sensor with micropillar working

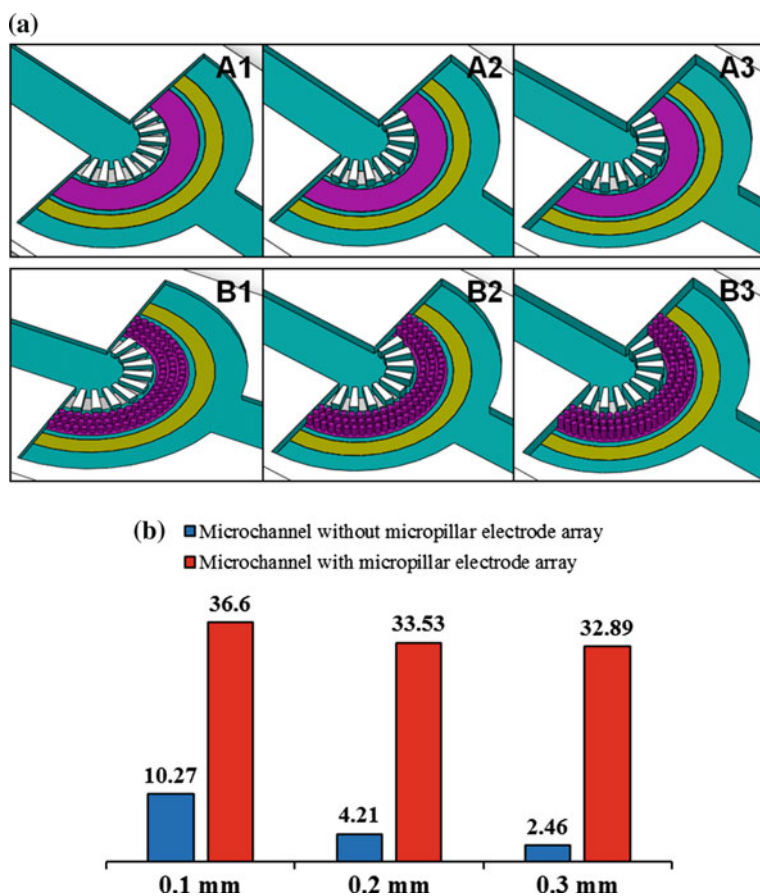


**Fig. 2.20** **a** Schematic drawings of the second simulation using the sensors with different pillar heights, 0.1 (Design B1), 0.2 (Design B2) and 0.3 (Design B3) mm. **b** Comparisons of species capture efficiency in terms of percentage (%) for the simulations under different height of the micropillar working electrode array

electrode array under different channel heights. Specifically, enhancement of species capture efficiency climbs up to 3.56, 7.96 and 13.37 times for the sensor with and without micropillar working electrode array when the pillar height is specified as 0.1, 0.2 and 0.3 mm, respectively. Such prodigious improvement is contributed by the fact that the micropillar working electrode array is able to protrude from the thick boundary layer, which makes the working electrode surface to be fully exposed to the flowing solution, thereby greatly enhancing the ion-collection efficiency. However, for the sensor without micropillar working electrode array, the flat electrode will be severely immersed in the boundary layer especially when the microfluidic channel is heightened, which retards the effective interaction/contact between the dissolved ions in the solution and the surface of the working electrode.

### 2.3.3 Characterization of the Sensor

Before evaluating the performance of the proposed sensor for heavy metal detection, the shark-inspired MEMS chemical sensor was carefully characterized after fabrication. The electrical connection between contact pads of each electrode and the connection of each micropillar electrode with respect to the contact pad were checked under a high precision probe station, as shown in Fig. 2.21a. The probe station is equipped with a high resolution optical microscope and two movable

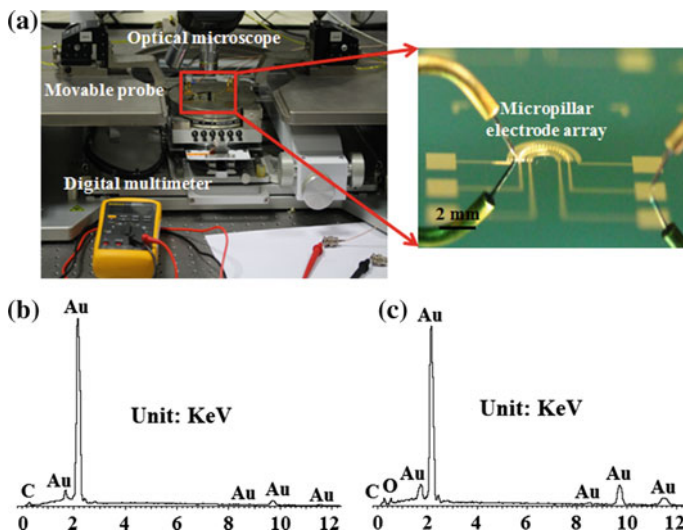


**Fig. 2.21** a Photograph of the high precision probe station to check electrical connection between each micropillar electrode and the contact pad. EDS spectrum of **b** top surface and **c** side surface of one micropillar electrode to show elemental composition in the unit of kilo-electronvolt (KeV) [19]. Reprinted with permission from Ref. [19]. Copyright (2015) IEEE

probes that can be finely adjusted in three dimensions. Digital multimeter was used to determine whether the measured resistance is in the range of the reference values. To further verify the presence of the gold layer, energy dispersive spectroscopy (EDS) analysis was implemented on the top surface and side surface of individual micropillar electrode, as shown in Fig. 2.21b, c, respectively. EDS spectrum characterization, a technique to investigate elemental composition of a sample surface, utilizes the fundamental principle that every element will emit a unique set of X-rays upon shining by a beam of high-energy charged particles. Seen from Fig. 2.21b, c, the EDS spectrums clearly indicate that both top surface and side surface of the micropillar electrode were coated with gold.

After investigating the surface properties of the micropillar working electrode array, the proposed sensor was packaged by soldering the contact pad of the working electrode to connection wire using conductive epoxy, followed by baking in the oven at 80 °C for three hours. Subsequently, non-conductive epoxy was used to shield all other regions of the sensor, leaving only the micropillar working electrode array together with the bottom flat working electrode to be exposed. Then the whole device was put into the oven to bake at 80 °C for one and half hours. Once packaging of the sensor was finished, cyclic voltammetry (CV) experiment was performed to check whether redox reaction can be precisely recorded by the micropillar working electrode array. The packaged MEMS chemical sensor, a commercial Ag/AgCl (3 Mol/L NaCl as inner electrolyte) reference electrode and a commercial platinum (Pt) counter electrode were immersed into the analytical grade solution, which had 2 mM/L potassium ferricyanide ( $K_3Fe(CN)_6$ ) and 0.2 Mol/L potassium chloride (KCl) as supporting electrolyte. The CV experiments were conducted with an initial and final potential of 0.6 V, switching potential of -0.2 V, and varying scan rate from 0.01 to 0.15 V/s. As shown in Fig. 2.22a, legible reduction and oxidation peaks are observed at the potential near 0.17 and 0.26 V irrespective of different scan

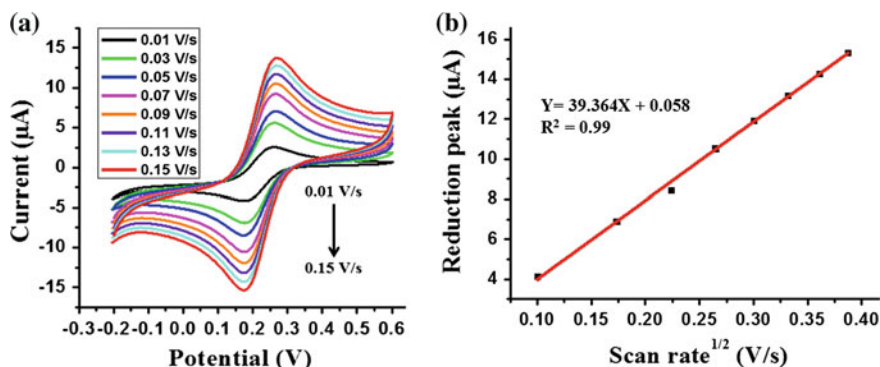


**Fig. 2.22** **a** Cyclic voltammograms using the sensor with micropillar working electrode array under different scan rates from 0.01 to 0.15 V/s. **b** The corresponding fitting curve of the magnitudes of the reduction peaks with respect to the square root of different scan rates. Reprinted with permission from Ref. [19]. Copyright (2015) IEEE

rates, indicating that redox reaction happened in the vicinity of the micropillar working electrode array were accurately tracked.

Since all the CV experiments were performed in the quiescent condition, the convection effect didn't contribute to the transport of ferricyanide ions to the surface of the micropillar working electrode array. Moreover, the migration effect, which is usually contributed by the presence of a electrical field, also didn't help the transport of electroactive ions as the concentration of the supporting electrolyte (0.2 Mol/L KCl) was 100 times higher than the one of the ferricyanide ions (2 mM/L  $\text{K}_3\text{Fe}(\text{CN})_6$ ). Hence, transportation of the ferricyanide ions to the electrode-solution interface was only controlled by the diffusion effect. Under this condition, according to the Randles-Sevcik equation [21], the peak current of CV experiment will be linearly related to the square root of the scan rate. Figure 2.22b shows the relationship between the magnitudes of the reduction peak currents and the square root of different scan rates (from 0.01 to 0.15 V/s). The fitting curve displays good linearity with a correlation coefficient of 0.99. These results exhibit promising capability of the proposed shark-inspired MEMS chemical sensor with micropillar working electrode array to be used as an electrochemical sensor for the application of environmental sensing.

### 2.3.4 Heavy Metal Detection with the Sensor

After comprehensively characterizing the shark-inspired MEMS chemical sensor, the performance of the proposed sensor for heavy metal detection was investigated by employing square wave anodic stripping voltammetry (SWASV). Diluted copper and lead solutions were prepared from 1000 mg/L standard stock solutions with deionized water collected from a Milli-Q system. SWASV experiments were performed by applying certain deposition potential for a period of time (deposition time). After the quiescent time, the voltammograms were recorded in a certain potential window under the square wave mode with optimal frequency, amplitude and step potential. Prior to next measurement, a conditioning potential was applied to remove any residual metal left on the surface of the micropillar working electrode array. For the detection of copper ions, the effect of deposition potential was evaluated from 0 to  $-0.5$  V with respect to the on-chip Ag/AgCl reference electrode. As shown in Fig. 2.23a, the stripping current was initially increased when the deposition potential changed from 0 to  $-0.3$  V, as more energy was provide for the preconcentration of copper ions on the working electrode surface. The highest current response was recorded at  $-0.3$  V. The peak current was decreased when deposition potential became more negative, which was mainly caused by the evolution of hydrogen. Deposition time ranging from 10 to 60 s was also studied in order to further optimize the experimental condition. As shown in Fig. 2.23b, a sharp increase was observed between 10 and 30 s. After that, the peak current reached to a plateau value and then dropped subsequently due to the saturation

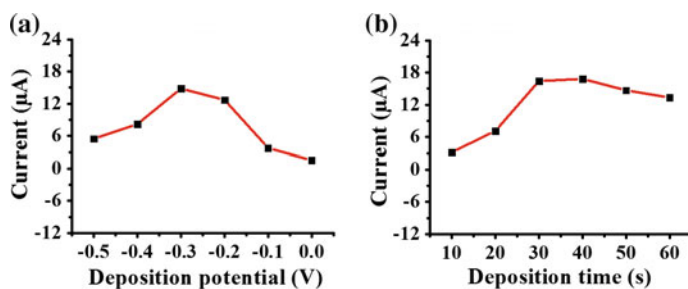


**Fig. 2.23** Effects of **a** deposition potential and **b** deposition time on the stripping current of 30 ppb copper ions with the shark-inspired MEMS chemical sensor [20]. Measurement parameters: deposition time of 30 s for **a**, deposition potential of  $-0.3$  V for **b**, frequency of 20 Hz, amplitude of 45 mV and step potential of 5 mV

effect. Therefore,  $-0.3$  V and 40 s were selected as the deposition potential and deposition time, respectively.

By continuously injecting the testing solution into the microfluidic channel, a series of SWASV were carried out with increased concentrations of copper ions from 10 to 110 ppb with 20 ppb increment. The obtained anodic stripping voltammograms are shown in Fig. 2.24a, where all stripping peaks are located around the potential of 0.05 V with respect to the on-chip Ag/AgCl reference electrode. Figure 2.24b displays the calibration curve between the magnitudes of the peak currents versus different copper concentrations, in which linear responses with a high analytical sensitivity of 32 nA/ppb are obtained. Limit of detection down to 0.4 ppb was also achieved by using the proposed chemical sensor.

As for the lead detection, SWASV experiments were conducted in the quiescent condition by increasing the lead concentrations from 10 to 100 ppb with 10 ppb increment. Experimental parameters such as frequency, amplitude and step

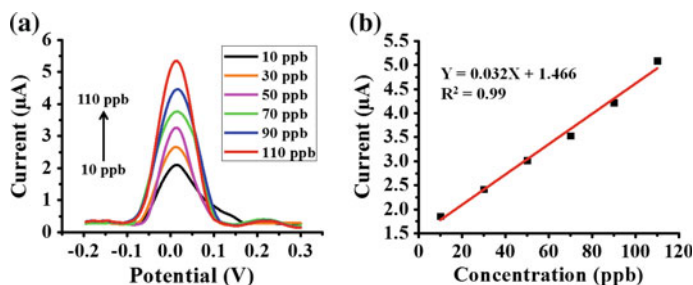


**Fig. 2.24** **a** Square wave anodic stripping voltammograms for increasing concentrations of copper ions from 10 to 110 ppb [20]. **b** The corresponding calibration curve of the stripping peak current versus the copper concentration [20]. Measurement parameters: deposition potential of  $-0.3$  V, deposition time of 40 s, frequency of 20 Hz, amplitude of 45 mV and step potential of 5 mV



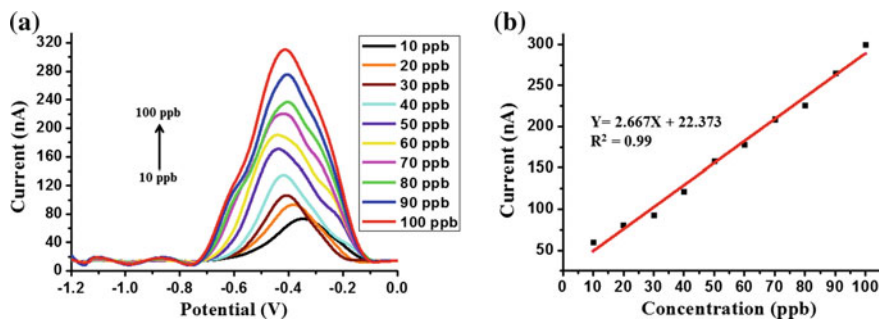


**Fig. 2.25** **a** Square wave anodic stripping voltammograms for increasing concentrations of lead ions from 10 to 100 ppb. **b** The corresponding calibration curve of the stripping peak current versus the lead concentration. Measurement parameters: deposition potential of  $-1.2$  V, deposition time of 5 min, frequency of 50 Hz, amplitude of 50 mV and step potential of 5 mV. Reprinted with permission from Ref. [19]. Copyright (2015) IEEE

potential of the square wave mode were changed accordingly. As shown in Fig. 2.25a, legible and well-defined stripping peaks are observed near the potential of  $-0.4$  V with respect to the on-chip Ag/AgCl reference electrode. A linear calibration curve, as shown in Fig. 2.25b, with an analytical sensitivity of 2.7 nA/ppb is attained and the limit of detection reached to 0.8 ppb without any involvement of magnetic/mechanical stirring of the testing solution.

## 2.4 Conclusions and Future Work

The olfactory sensing system possessed by both terrestrial animals and aquatic animals manifests almost equivalent level of outstanding capacity for air-borne and water-borne odorant molecules. Tremendous sensitivity as well as high selectivity is attributed to the special anatomical structure of the olfactory receptor cells along with the sophisticated arrangement of the olfactory neurons. Such compelling sensation system has provided a number of inspirations for researchers in both academic and industrial areas to develop chemical sensors/systems to procure comparable sensing capabilities. In this chapter, we have briefly introduced some artificial sensors/systems that are focusing on the bio-inspiration and/or biomimicry of certain functions, structures or layouts of the terrestrial animals' olfactory sensory organs. We have also elaborated the development of a MEMS chemical sensor to mimic both morphological and functional merits of the aquatic animals' olfactory sensing system for the application of heavy metal detection. Although some of these attempts have already achieved rather exciting experimental outcomes, endeavors in the future should move forward to imitate the entire hierarchy of the olfactory system especially the fascinating functional and neural configurations.

## References

1. Press Release (2016) Nobelprize.org. Nobel Media AB 2014. [http://www.nobelprize.org/nobel\\_prizes/medicine/laureates/2004/press.html](http://www.nobelprize.org/nobel_prizes/medicine/laureates/2004/press.html). Accessed 06 Feb 2016
2. Wyszynski B, Nakamoto T (2009) Linking biological and artificial olfaction: biomimetic quartz crystal microbalance odor sensors. *IEEE T Electr Electr* 4(3):334–338
3. Zeiske E, Theisen B, Breucker H (1994) The olfactory organ of the hardhead sea catfish, *Arius felis* (L.): gross morphology and fine structure. *Acta Zool* 75(2):115–123
4. Hamdani EH, Doving KB (2007) The functional organization of the fish olfactory system. *Prog Neurobiol* 82(2):80–86
5. Schluessel V, Bennett MB, Bleckmann H, Blomberg S, Collin SP (2008) Morphometric and ultrastructural comparison of the olfactory system in elasmobranchs: the significance of structure-function relationships based on phylogeny and ecology. *J Morphol* 269(11):1365–1386
6. Cox JPL (2008) Hydrodynamic aspects of fish olfaction. *J R Soc Interface* 5(23):575–593
7. Zeiske E, Theisen B, Gruber SH (1987) Functional morphology of the olfactory organ of two carcharhinid shark species. *Can J Zool* 65(10):2406–2412
8. Kottapalli AGP, Bora M, Asadnia M, Miao JM, Venkatraman SS, Triantafyllou M (2016) Nanofibril scaffold assisted MEMS artificial hydrogel neuromasts for enhanced sensitivity flow sensing. *Sci Rep* 6:19336
9. Asadnia M, Kottapalli AGP, Miao JM, Warkiani ME, Triantafyllou MS (2015) Artificial fish skin of self-powered micro-electromechanical systems hair cells for sensing hydrodynamic flow phenomena. *J R Soc Interface* 12(111):20150322
10. Kottapalli AGP, Asadnia M, Miao JM, Triantafyllou M (2014) Touch at a distance sensing: lateral-line inspired MEMS flow sensors. *Bioinspir Biomim* 9(4):046011
11. Asadnia M, Kottapalli AGP, Haghighi R, Cloitre A, Alvarado PV, Miao J, Triantafyllou M (2015) MEMS sensors for assessing flow-related control of an underwater biomimetic robotic stingray. *Bioinspir Biomim* 10(3):036008
12. Wang N, Kanhere E, Miao JM, Triantafyllou MS (2016) Miniaturized chemical sensor with bio-inspired micropillar working electrode array for lead detection. *Sens Actuators, B* 233:249–256
13. Di Natale C, Martinelli E, Paolesse R, D'Amico A, Filippini D, Lundstrom I (2009) An artificial olfaction system based on the optical imaging of a large array of chemical reporters. *Sens Actuators, B* 142(2):412–417
14. Wang LC, Tang KT, Chiu SW, Yang SR, Kuo CT (2011) A bio-inspired two-layer multiple-walled carbon nanotube–polymer composite sensor array and a bio-inspired fast-adaptive readout circuit for a portable electronic nose. *Biosens Bioelectron* 26(11):4301–4307
15. Illustrated Information (2016) Nobelprize.org. Nobel Media AB 2014. [http://www.nobelprize.org/nobel\\_prizes/medicine/laureates/2004/illpres/illpres.html](http://www.nobelprize.org/nobel_prizes/medicine/laureates/2004/illpres/illpres.html). Accessed 15 Feb 2016
16. Cui Y, Kim SN, Naik RR, Mcalpine MC (2012) Biomimetic peptide nanosensors. *Acc Chem Res* 45(5):696–704
17. Kaupp UB (2010) Olfactory signalling in vertebrates and insects: differences and commonalities. *Nat Rev Neurosci* 11(3):188–200
18. Yusko EC, Johnson JM, Majd S, Prangkio P, Rollings RC, Li J, Yang J, Mayer M (2011) Controlling protein translocation through nanopores with bio-inspired fluid walls. *Nat Nanotechnol* 6(4):253–260
19. Wang N, Kanhere E, Triantafyllou MS, Miao JM (2015) Shark-inspired MEMS chemical sensor with epithelium-like micropillar electrode array for lead detection. *Proceeding of solid-state sensors. Actuators and Microsystems (TRANSDUCERS)*, Anchorage, Alaska, U.S.A., pp 1464–1467

20. Wang N, Kanhere E, Triantafyllou MS, Miao JM (2015) Copper detection with bio-inspired MEMS-based electrochemical sensor. Proceeding of miniaturized systems for chemistry and life sciences. Gyeongju, Korea, pp 23–25
21. Monk PMS (2001) Fundamentals of electroanalytical chemistry. Wiley, New York

Biomimetic Microsensors Inspired by Marine Life

Kottapalli, A.G.P.; Asadnia, M.; Miao, J.; Triantafyllou, M.S.

2017, IX, 112 p. 86 illus., 75 illus. in color., Softcover

ISBN: 978-3-319-47499-1